
Article:
Cristoforetti, G., Hume, E., Agarwal, S. et al. (28 more authors) (2025) Investigation of ruling parameters on the growth of side and back stimulated Raman scattering in inhomogeneous plasmas at shock ignition laser intensity. Matter and Radiation at Extremes. 045401. ISSN: 2468-080X

https://doi.org/10.1063/5.0257022

LETTER | JULY 02 2025

Investigation of ruling parameters on the growth of side and back stimulated Raman scattering in inhomogeneous plasmas at shock ignition laser intensity

G. Cristoforetti ; E. Hume ; S. Agarwal ; D. Batani ; M. Cervenak ; P. Devi ; R. Dudzak ; D. Ettel ; P. Gajdos ; K. Glize ; S. Jelinek ; L. Juha ; P. Koester ; M. Krupka ; M. Krus ; H. Larreur ; G. Malka ; D. Mancelli ; P. E. Masson-Laborde ; A. Morace; Ph. Nicolai ; O. Renner ; D. Singappuli ; S. Singh ; M. Tatarakis ; X. Yuan ; Y. Wang ; N. Woolsey ; J. Zhang ; X. Zhao; L. A. Gizzi

Matter Radiat. Extremes 10, 045401 (2025)
https://doi.org/10.1063/5.0257022

Matter and Radiation at Extremes

LETTER

pubs.aip.org/aip/mre

Investigation of ruling parameters on the growth of side and back stimulated Raman scattering in inhomogeneous plasmas at shock ignition laser intensity

Cite as: Matter Radiat. Extremes 10, 045401 (2025); doi: 10.1063/5.0257022
Submitted: 8 January 2025 • Accepted: 31 May 2025 •
Published Online: 2 July 2025

G. Cristoforetti,[1,a)] E. Hume,[1] S. Agarwal,[2,3] D. Batani,[4] M. Cervenak,[5] P. Devi,[2,3] R. Dudzak,[2,5] D. Ettel,[2,6] P. Gajdos,[5] K. Glize,[7,8,9] S. Jelinek,[2,3,5] L. Juha,[2] P. Koester,[1] M. Krupka,[2,5,10] M. Krus,[5] H. Larreur,[4,11] G. Malka,[4] D. Mancelli,[12,13] P. E. Masson-Laborde,[14,15] A. Morace,[2] Ph. Nicolai,[4] O. Renner,[2,5,16] D. Singappuli,[4] S. Singh,[2,5,17] M. Tatarakis,[12,13] X. Yuan,[8,9] Y. Wang,[18] N. Woolsey,[18] J. Zhang,[8,9,19] X. Zhao,[8,9,18] and L. A. Gizzi[1]

AFFILIATIONS

[1]ILIL, CNR-INO, Pisa, Italy
[2]Institute of Physics of the CAS, Prague, Czech Republic
[3]Faculty of Mathematics and Physics, Charles University, Prague, Czech Republic
[4]Université de Bordeaux, CNRS, CEA, CELIA, Talence 33405, France
[5]Institute of Plasma Physics of the CAS, Prague, Czech Republic
[6]Faculty of Mechatronics, Informatics and Interdisciplinary Studies, TUL, Liberec, Czech Republic
[7]Rutherford Appleton Lab, CLF, Didcot, United Kingdom
[8]Key Laboratory for Laser Plasmas (MoE), School of Physics and Astronomy, SJTU, Shanghai, China
[9]CICIFSA, SJTU, Shanghai, China
[10]Faculty of Nuclear Science and Physical Engineering, Czech Technical University, Prague, Czech Republic
[11]Departamento de Física fundamental, Facultad de Ciencias, Universidad de Salamanca, Salamanca, Spain
[12]Institute of Plasma Physics and Lasers-IPPL, University Research and Innovation Center, Hellenic Mediterranean University, Rethymno, Greece
[13]Department of Electronic Engineering, Hellenic Mediterranean University, Chania, Greece
[14]CEA, DAM, DIF, F-91297 Arpajon, France
[15]Université Paris-Saclay, CEA, Laboratoire Matière en Conditions Extrêmes, 91680 Bruyères-le-Châtel, France
[16]The Extreme Light Infrastructure ERIC, ELI Beamlines Facility, Dolni Brezany, Czech Republic
[17]Faculty of Electrical Engineering, Czech Technical University, Prague, Czech Republic
[18]York Plasma Institute, University of York, York, United Kingdom
[19]Beijing National Laboratory for Condensed Matter Physics, IOP, CAS, Beijing, China

[a)]**Author to whom correspondence should be addressed:** gabriele.cristoforetti@cnr.it

ABSTRACT

Recent experiments at the National Ignition Facility and theoretical modeling suggest that side stimulated Raman scattering (SSRS) instability could reduce laser–plasma coupling and generate considerable fluxes of suprathermal hot electrons under interaction conditions envisaged for direct-drive schemes for inertial confinement fusion. Nonetheless, SSRS remains to date one of the least understood parametric instabilities. Here, we report the first angularly and spectrally resolved measurements of scattered light at laser intensities relevant for the shock ignition scheme ($I \sim 10^{16}$ W/cm^2), showing significant SSRS growth in the direction perpendicular to the laser polarization. Modification of the focal spot shape and orientation, obtained by using two different random phase plates, and of the density gradient of the plasma, by utilizing exploding foil targets of different thicknesses, clearly reveals a different dependence of backward SRS (BSRS) and SSRS on experimental

parameters. While convective BSRS scales with plasma density scale length, as expected by linear theory, the growth of SSRS depends on the spot extension in the direction perpendicular to laser polarization. Our analysis therefore demonstrates that under current experimental conditions, with density scale lengths $L_n \approx 60$–$120\ \mu$m and spot sizes FWHM ≈ 40–100 μm, SSRS is limited by laser beam size rather than by the density scale length of the plasma.

 https://doi.org/10.1063/5.0257022

The coupling of an intense laser pulse ($I \gtrsim 10^{14}$ W/cm^2) with a plasma corona is strongly affected by the onset of laser–plasma instabilities (LPIs). In both indirect-drive and direct-drive schemes of inertial confinement fusion (ICF), this can influence the efficiency and symmetry of fuel compression, and ultimately the fusion gain. Among these instabilities, backward stimulated Raman scattering (BSRS), where laser light is scattered by an electron plasma wave (EPW) in the backward direction, has been thoroughly investigated over the last 40 years. Conversely, however, side stimulated Raman scattering (SSRS) has been hardly investigated and remains poorly understood. In SSRS, laser light is scattered by an EPW in a direction perpendicular to the electron density gradient and is successively refracted to lower densities, finally exiting the plasma at large angles [Fig. 1(d)], as described below.

Early theoretical work on SSRS, dating back to the 1970s,[1–3] immediately revealed the difficulty in describing a process that can have both an absolute character, with eigenmodes temporally growing at a single point, and a convective character, with wave packets growing in a resonance region along the scattered light trajectory. In addition, convective growth occurs near the turning point of scattered light where the Wentzel–Kramers–Brillouin (WKB) approximation fails,[4] making theoretical analysis less straightforward.[3] The first coherent picture of SSRS, derived for infinite transverse extension and negligible Landau damping of the EPW, was proposed by Mostrom and Kaufman,[3] showing that wave packets rapidly grow and saturate owing to refraction out of the resonance zone, while eigenmodes grow more slowly and prevail at later times. In this model, both the resonance length L_{res} of the wave packets, and thus their gain, and the eigenmodes threshold scale with the electron density scale length $L_n \equiv n/(dn/dz)$.

Although early work predicted a massive and threatening impact on ICF performance, only a few experiments in the 1980s[5–7] succeeded in detecting a weak SSRS signal, which led to a rapid halt to its investigation. Possible reasons for these detection failures could be the finite size of the laser beam, limiting the growth of the instability, the high collisional absorption of scattered light before leaving the plasma, and the difficulty in measuring light scattered over a wide solid angle. Recent observations of strong SSRS at the NIF,[8–10] OMEGA-EP[11] and SG-II UP,[12–15] driven at laser intensity in the range 10^{14}–10^{15} W/cm^2, stimulated, however, renewed effort aimed at its experimental characterization. At the same time, recent theoretical work has explored cases of strong Landau damping,[10] closer to the expected ICF conditions, and has quantified the corrections due to the limited size of the laser beam.[3,16] The k-space theory, finally, has provided a more complete and coherent framework of SSRS,[17,18] reproducing the extreme cases of cold and hot plasmas found in previous papers.

One difficulty in SSRS characterization, and even more in the measurement of its reflectivity, is due to its intrinsic 3D geometry, since the intensity of the scattered light is expected to depend on both the polar angle, i.e., the angle with respect to the density gradient, because of light refraction into the plasma, and on the azimuthal angle, i.e., the angle with respect to the plane of polarization. In the following, the directions in the focal plane that are parallel and perpendicular to the laser polarization will be named the p-direction and s-direction, respectively. Correspondingly, the P-plane and the S-plane will respectively indicate the plane of polarization and the plane perpendicular to it that includes the laser axis.

Following a clear observation of SSRS in a previous experiment at the Prague Asterix Laser System (PALS),[19] we present here the first angularly resolved measurements of SSRS driven at laser intensities ~10^{16} W/cm^2 that are relevant for the shock ignition scheme for ICF. The measurements, obtained with the specifically designed Octopus diagnostic, clearly show the dependence of SSRS on the laser spot extent in the s-direction. We also demonstrate that, differently from BSRS, SSRS is here unaffected by the density scale length of the plasma.

The experiment was carried out at PALS by focusing a single laser pulse ($\lambda_0 = 438$ nm, $\tau \approx 300$ ps) at normal incidence on plane targets by means of an $f/2$ lens. To investigate the effects of focal spot size and orientation with respect to laser polarization, two different random phase plates (RPPs) were used, providing either a Gaussian circular spot (RPP1, FWHM ≈ 60 μm) or an elliptical super-Gaussian spot (RPP2, FWHM1 ≈ 40 μm, FWHM2 ≈ 100 μm), resulting in comparable peak laser intensities in the range $(1.0$–$1.4) \times 10^{16}$ W/cm^2. Since SSRS is expected to grow more strongly along the s-direction,[2,16] during the experiment RPP2 was rotated to align the longer axis along (configuration RPP2-P) and across (RPP2-S) the laser polarization [Figs. 1(a)–1(c)].

The dependence of LPI on density scale length was investigated by varying the target thickness, going from "thick" multilayer targets—with 20, 60, and 100 μm Parylene-C ablators, followed by a 7 μm Cu tracer layer—down to "thin" Parylene-N foils of 2.16, 2.99, and 5.41 μm (hereinafter referred to as 2, 3 and 5 μm foil targets). Target thickness was measured by spectral reflectance and contact probe techniques with an uncertainty <10 nm. A ~50 nm Al coating was deposited on the laser side of both the Parylene-C and Parylene-N ablators to avoid laser propagation at early times of interaction. It is worth noting that for the "thick" targets, new material is ablated at any time during laser irradiation, and so the plasma density profile does not depend on the target thickness; accordingly, no substantial differences were observed in the features of LPI for the various thick targets in this experiment. In the following, we therefore gather them all as "thick target" shots. By contrast, for the so-called "thin" targets, the laser is expected to burn through the foil at a certain time, depending on the initial thickness, when the peak electron density falls below the critical density n_c of the laser light; from that

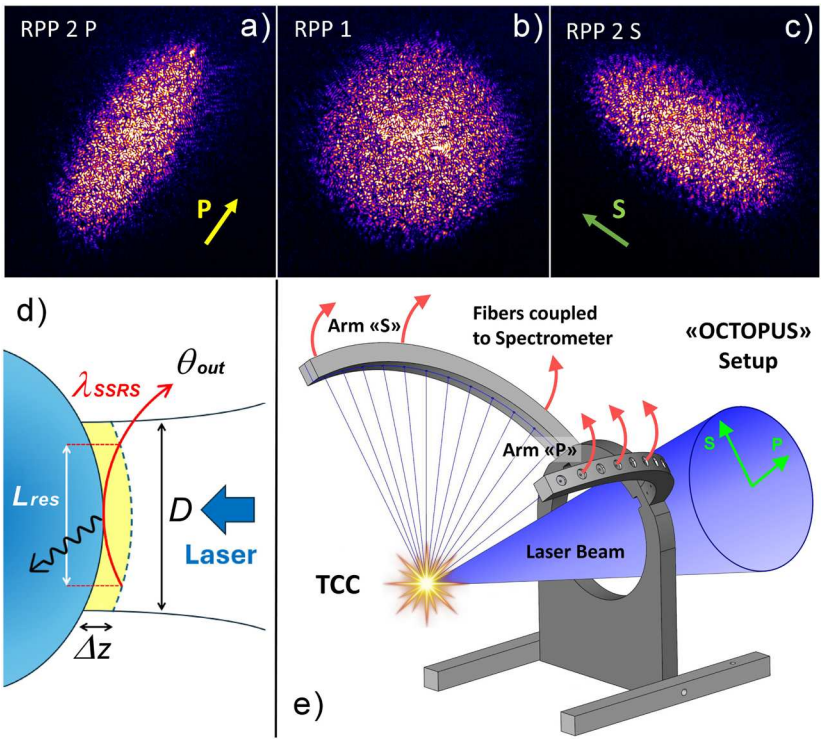

FIG. 1. (a)–(c) Images of focal spots obtained in configurations corresponding to minimum (RPP2-P), intermediate (RPP1), and maximum (RPP2-S) SSRS growth. (d) Scheme of convective SSRS driven in an inhomogeneous plasma by a laser beam of size D. L_{res} and Δz are the length and thickness, respectively, of the resonance region, λ_{SSRS} is the SSRS light wavelength, and θ_{out} is the exit angle from the plasma. Here, the scattered light (λ_{SSRS}) builds up in the resonance region of length L_{res} and thickness Δz, leaving the plasma at an angle θ_{out}. (e) Setup of Octopus fiber-holder.

time, no more material is ablated and the hydrodynamic evolution is determined by plasma expansion alone.[20]

The expected plasma conditions during laser interaction were investigated by means of hydrodynamic simulations with the 2D code CHIC,[21] for the circular laser spot [Fig. 2(a)], and with the 3D code Troll[22] for comparing the differences between circular and elliptical spots [Fig. 2(b)]; the discrepancies in the temperatures and density scale length values obtained with the two geometries were below 5%. Simulations show that L_n increases when the target thickness decreases from thick targets down to 2 μm [Fig. 2(a)]. At a time ≈150 ps after the laser peak and in the density region $n = 0.12n_c$, for which SRS instability is stronger, the calculated values of L_n are 63, 76, 86, and 115 μm for thick targets and 5, 3, and 2 μm foils, respectively. For thin foil targets, the laser burns through before the end of the laser pulse [Fig. 2(a)], making L_n locally diverge at longer times and higher densities.

BSRS was characterized by full-aperture beam (FAB) calorimetry, using a Gentec pyroelectric detector, and FAB time-resolved spectroscopy, using a Czerny–Turner ISOPLANE-160 spectrograph (Princeton Instruments) with 150 or 300 lines/mm gratings coupled to a Hamamatsu C7700 optical streak camera. SSRS was measured by the angularly resolved Octopus spectrometer [Fig. 1(e)], consisting of two circular aluminum arms, each holding 12 optical fibers placed at polar angles going from 23° to 90° to the laser beam axis. The two arms, aligned in planes at 10° (hereinafter "P") and at 80° (hereinafter "S") to the laser polarization, allowed simultaneous measurement of Raman spectra at different polar angles in planes near-parallel (P-plane) and near-perpendicular (S-plane) to the laser polarization. The 24 fibers were bundled to the entrance slit of a MS257 Oriel 1/4-m imaging spectrometer coupled to a 14-bit CCD, resolving SSRS spectra in the range 600–910 nm. A white light source of known emissivity was placed at the target chamber center (TCC), allowing absolute energy calibration for the signal measured by each fiber; the calibration procedure was the same as described in Ref. 13.

A typical angularly resolved spectrum obtained using the RPP1 plate and a thick target is shown in Fig. 3; the corresponding values of SRS scattered energy at each angle, integrated in the spectral range 600–800 nm and measured in joules per solid angle (J/sr), is reported in Fig. 4(c) for the P- and S-planes.

The SSRS signal can be clearly recognized in the diagonal traces visible in both planes. Here, the SRS spectra measured at each angle are different, showing a peak signal moving to shorter wavelengths for larger polar angles. This trend is a signature of SSRS, where a definite relation between the wavelength λ_{SSRS} of the scattered light and its exit angle θ_{out} holds. This light is scattered in the region $0.07n_c$–$0.18n_c$ as obtained assuming a ≈2 keV plasma temperature given by hydrodynamic simulations [Fig. 2(a)]. The experimental λ_{SSRS}–θ_{out} relation (blue dashed line), however, departs from the analytical formula $\theta_{out} = \arctan\sqrt{\omega_0^2/\omega_p^2 - 2\omega_0/\omega_p}$ (black dots), where ω_0 and ω_p are the laser light and plasma frequencies, which is obtained by considering light refraction in a 1D plasma profile;[16] it is likely that the trajectory of SSRS light into the plasma is here affected by the curvature of the isodensity lines into the plasma. We finally note that the signal in the S-plane is much stronger–by about two

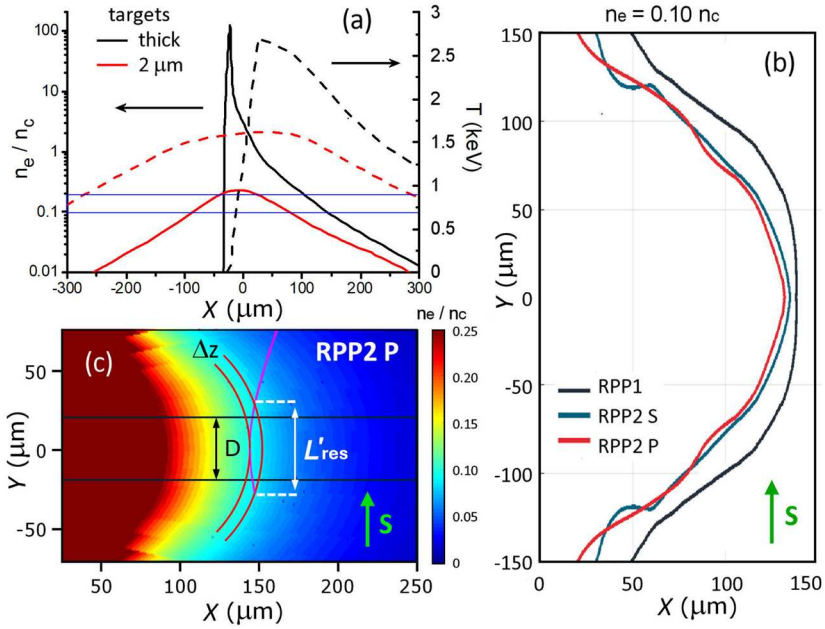

FIG. 2. (a) longitudinal profiles of electron density (solid lines) and temperature (dashed lines) obtained by the 2D CHIC code for the irradiation of a thick and a 2 μm foil target with circular laser spot (RPP1) at a time 100 ps after the laser peak. The blue rectangle represents the density region where SRS is driven. (b) Radial isodensity profiles at $n = 0.10n_c$ along the s-direction obtained by the 3D code Troll for the irradiation of a thick target with RPP1, RPP2P, and RPP2S geometries at a time 100 ps after the laser peak. (c) Ray-tracing simulation of light scattered along the s-direction at $n = 0.12n_c$ for RPP2P geometry, calculated on the density map obtained by the 3D Troll code at a time of 100 ps after the laser peak, showing the resonance thickness Δz and length L'_{res}.

orders of magnitude [Fig. 4(c)]–than that in the P-plane, as expected from theory.[2]

In addition to SSRS, Fig. 3 shows a signal at near-backscattering angles, with comparable intensities in the P- and S-planes. This spectrum (e.g., that observed at $\theta_{out} = 23°$) is consistent with that measured by the FAB spectrometer ($\theta_{out} < 14°$), showing a BSRS signal peaked at $\lambda \approx 700$ nm, and the $\omega_0/2$ doublet, which is a signature of two-plasmon decay (TPD) instability [Fig. 5(a)]. This shows that BSRS extends in the near-backscattering cone (n-BSRS) and progressively fades for larger polar angles. Figure 3 also shows that the $\omega_0/2$ feature disappears rapidly with increasing polar angle, owing to the stronger refraction of light generated in the $n_c/4$ region. The streaked spectra in the FAB line [Fig. 5(b)] show that both BSRS and TPD are driven during the trailing part of the laser pulse at times ~100–150 and ~200 ps, respectively, after its peak. A similar result was obtained and modeled for BSRS in a previous experiment,[23,24] showing that the strongest growth is obtained for larger values of L_n, i.e., at late times, and while the laser intensity is still significant; the late onset of TPD is therefore unexpected. Calorimetric measurements in the FAB cone obtained for circular spots on thick targets yielded a BSRS reflectivity of (0.020 ± 0.005)%, similar to the levels measured in previous work under similar conditions.[23,24] We note that L_n is here an order of magnitude smaller than that expected in an ICF plasma corona, which explains the low reflectivity measured in the experiment. The total reflectivity of SSRS is not measured here.

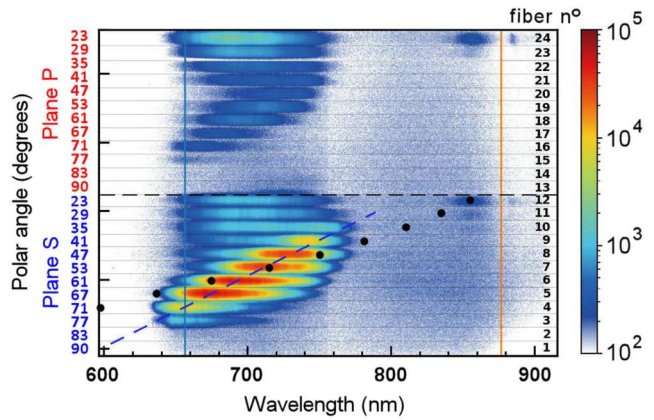

FIG. 3. Angularly resolved spectrum obtained by focusing a laser pulse ($I = 1.2 \times 10^{16}$ W/cm^2) onto a circular focal spot (RPP1) on a thick target. The signal is plotted on a logarithmic scale, and the polar angle is zero in the backscattering direction. The black dots indicate the λ_{SSRS}–θ_{out} relation expected for a 1D plasma density profile, while the dashed blue line is the experimental relation. The vertical orange line indicates the $\omega_0/2$ wavelength.

The dependence of SSRS on focal spot shape is revealed in Fig. 6, where angularly resolved spectra measured from thick targets with RPP2-P and RPP2-S configurations are shown; the corresponding spectrally integrated SRS scattered energies (J/sr) in the P- and S-planes are reported in Figs. 4(a) and 4(e).

Although the peak laser intensity $I \approx 1.2 \times 10^{16}$ W/cm^2 is comparable to that of Fig. 3, clear differences emerge from comparison of the spectra. First, the SSRS spectra observed for the RPP2-P shots are limited to wavelengths >700 nm, corresponding to densities higher than $0.13n_c$. Second, the deviation of the experimental λ_{SSRS}–θ_{out} relation from that expected in a 1D plasma geometry is more accentuated, producing a mixture of SSRS and n-BSRS signals at small polar angles; in Fig. 6(a), for example, a strong SSRS peak at $\lambda \approx 750$ nm is observed at $\theta = 23°$, as plotted in Fig. 7(a). FABS

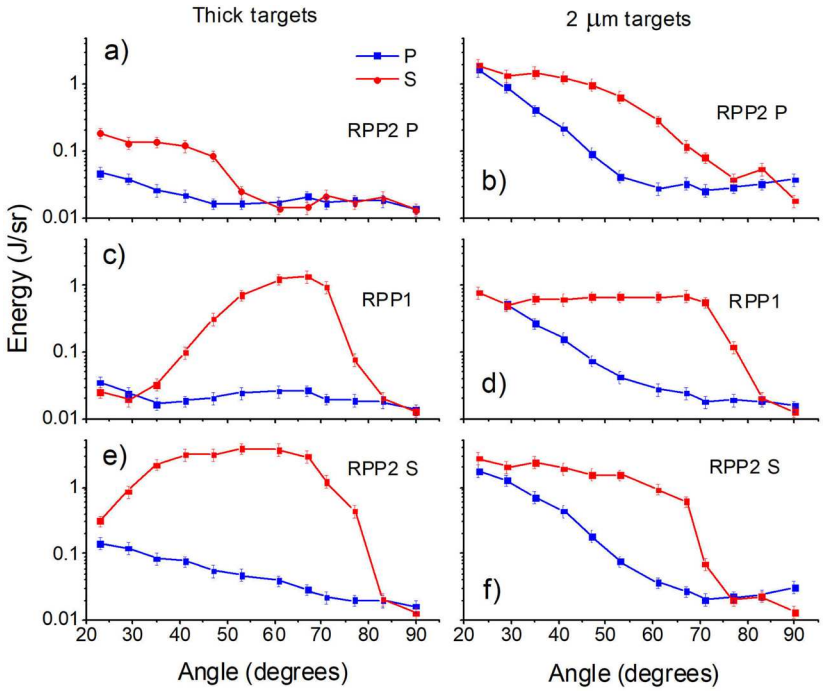

FIG. 4. SRS scattered energy measured in the P- and S-planes in different shots. The left and right columns show the results from shots with thick and 2 μm foil targets, respectively, while the rows correspond to shots with RPP2-P, RPP1, and RPP2-S, moving from top to bottom. Thus, the density scale length of the plasma increases from left to right, while the spot extent in the S-direction increases from top to bottom. The uncertainty, represented by the error bars, is 20% of the calculated energies.

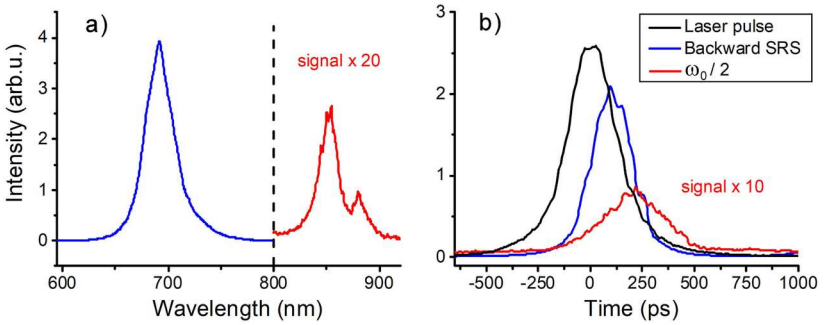

FIG. 5. (a) Time-integrated spectrum and (b) time-resolved intensity of BSRS and $\omega_0/2$ measured by the FAB spectrometer.

spectra measured in RPP2-P shots consistently exhibited a peak at shorter wavelengths, produced by BSRS, and an additional signal at longer wavelengths, corresponding to the SSRS peak observed at near-backscattering angles. The identification of the origin of the second peak in the streaked spectra allowed us to determine the time of SSRS emission, which is ~100–200 ps after the laser peak; the SSRS growth is therefore concomitant with those of BSRS and TPD. The strong refraction of SSRS light toward near-backscattering angles could be produced by a significant curvature of isodensity lines into the plasma as shown in Fig. 2(c); the observation of scattered light at lower polar angles could be produced, for example, by the onset of SSRS at the borders of the laser beam, where the light incidence is oblique with respect to the isodensity surface, and the side light is scattered in the backward SSRS configuration.[25] In the case of shots using the RPP2-S configuration, the maximum intensity of SSRS is comparable to that obtained with RPP1; here, however, the spectrum observed at each polar angle extends to shorter wavelengths, as can clearly be seen on comparing the curves of scattered energy in the S-planes in Figs. 4(c) and 4(e). These circumstances make a clear distinction from n-BSRS more difficult. This result could be explained by refractive effects or by the excitation of SRS in a broader range of angles with respect to the density gradient, going from 90° (SSRS) down to n-BSRS. Detailed modeling of SSRS growth into realistic hydrodynamic plasma maps by using suitable ray-tracing codes[11] is needed to reproduce the observed results.

A further difference revealed by comparison of Figs. 3 and 6 is that the intensity of SSRS is significantly lower in the RPP2-P configuration than in the RPP1 case, while it is slightly higher in the RPP2-S shots. For thick targets, the value obtained by adding up the spectrally integrated SSRS signals in all the fibers is in fact a factor ~10 lower for RPP2-P shots and ~2 higher for RPP2-S shots. Since

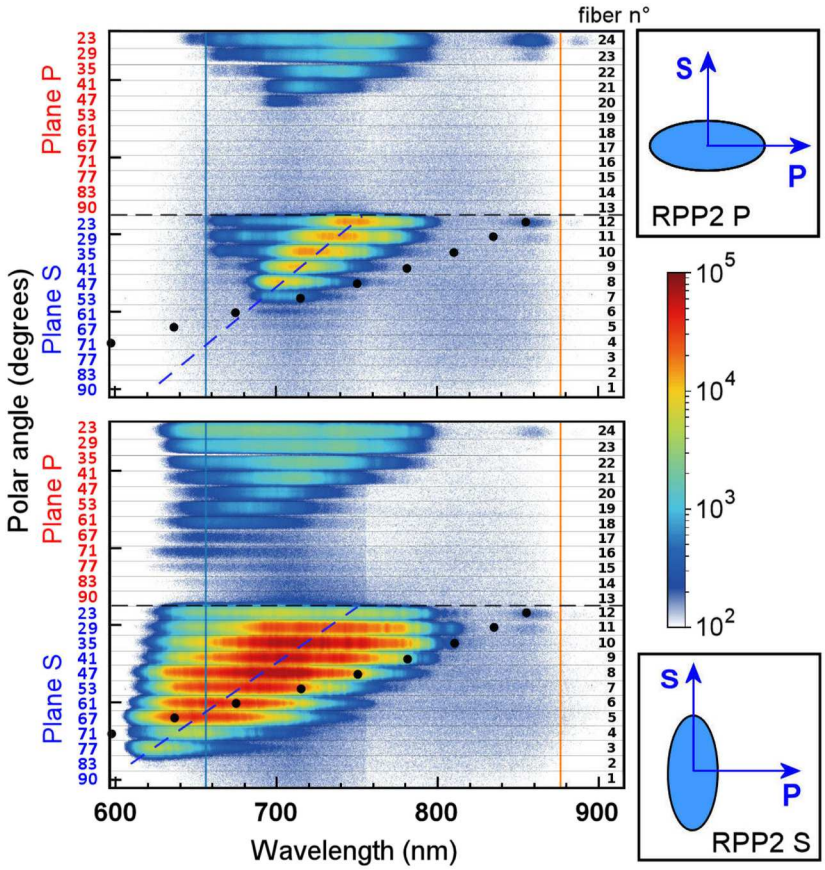

FIG. 6. Angularly resolved spectra from thick targets obtained with the elliptical focal spot in RPP2-P (top) and RPP2-S (bottom) configurations. In both shots, the peak laser intensity is comparable to that of Fig. 3. The marks have the same meaning as in Fig. 3.

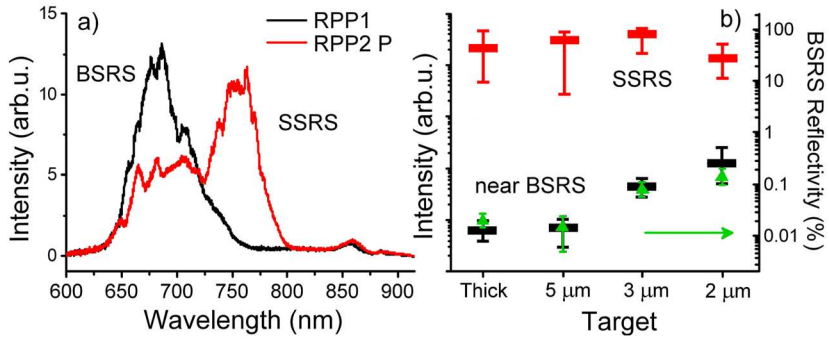

FIG. 7. (a) n-BSRS spectra at $\theta = 23°$ extracted from the P-planes of Fig. 3 (RPP1) and Fig. 6 (RPP2-P). (b) Average intensities of n-BSRS and SSRS obtained in RPP1 shots for different targets. The values, not comparable with each other, were calculated by integrating the spectrum at $\theta = 23°$ in the P-plane and by summing up the SSRS signal at all angles in the S-plane, respectively. BSRS reflectivities measured in the FAB cone are also reported (green triangles). The vertical lines represents the standard deviation of the statistical ensembles.

the density scale length, calculated on the central axis, is comparable in all cases, this suggests that SSRS growth is here restricted by the size of the spot in the S-direction.

This hypothesis can be corroborated by comparing the resonance length L_{res} of SSRS with the size of the focal spot D in the three irradiation configurations. In this experiment, the Landau damping of the EPW is negligible for $n > 0.1n_c$ (corresponding to $\lambda_{SSRS} > 640$ nm), implying that the convective growth of SSRS is limited by the refraction of scattered light out of the resonance zone, where the matching conditions of energy and momentum are fulfilled. Following the model of Mostrom and Kaufmann,[3] L_{res} can be estimated as the distance traveled by the wave packet at

velocity $v_g/2$, where v_g is the group velocity of the scattered light, during the time of saturation t_s of the wave packet growth [Eq. (2c) in Ref. 3]; for a density of $0.14n_c$ (corresponding to λ_{SSRS} = 700 nm), we then obtain a resonance region of thickness $\Delta z \approx 6.7$ μm and length $L_{res} \approx 120$ μm, traveled in a time $t_s \approx 700$ fs. These values are derived for a 1D plasma, depend linearly on L_n, and are calculated for thick target shots at a time 150 ps after the laser peak. For a finite focal spot size, however, L_{res} can be reduced by the plasma curvature if $\rho_{SSRS} \gtrsim \rho_{2D}$, where $\rho_{SSRS} = 2L_n[1 - (\omega_p/\omega_s)^2]/(\omega_p/\omega_s)^2$ is the radius of curvature of the scattered light trajectory (of frequency ω_s) in a 1D plasma, and ρ_{2D} is the radius of curvature of isodensity lines in the plasma. In that case, the scattered light moves out of the resonance region at earlier times and the growth stops at a reduced resonance length L'_{res}. In the case of a 1D plasma, the SSRS wave-packet saturation is produced by the density change corresponding to a longitudinal movement equal to the resonance thickness Δz. The value of L'_{res} in a curved plasma can be estimated by calculating the transverse size needed by a scattered light ray, refracting in a spherical plasma with the same density scale length value, to undergo the same density decrement. Using this procedure, we obtain $L'_{res} \approx L_{res}(1 + \rho_{SSRS}/\rho_{2D})^{-1/2}$.

Hydrodynamic simulations show that the radius of curvature ρ_{2D} of the isodensity lines depends on the time and the electron density considered. For $n = 0.14n_c$ (corresponding to λ_{SSRS} = 700 nm) at a time 150 ps after the laser peak, we obtain $\rho_{2D} \approx 200$ μm and $\rho_{2D} \approx 110$ μm for RPP1 and RPP2, respectively. It is interesting to note that the profile along the two axes in the RPP2 plasma is similar, despite the elliptical spot, as shown in Fig. 2(b) for $n_e = 0.10n_c$; this effect results from the expansion of the plasma making the profile in the transverse plane quite isotropic at later times of interaction. The above ρ_{2D} values correspond to resonance lengths of $L'_{res} \approx 80$ μm and $L'_{res} \approx 70$ μm for the RPP1 and RPP2 cases, respectively. In addition to plasma curvature, the growth of the wave packet is obviously confined by the finite size D of the beam in the S-direction. We can therefore conclude that the gain $\Gamma_{SSRS} \propto \min(D, L'_{res}, L_{res})$, where the dependence on L_n is lost if the beam size or the plasma curvature prevails.[3] Assuming $D \approx$ FWHM of the laser spot, calculated along the S-direction, we note that for the RPP2-P and RPP1 shots, $\Gamma_{SSRS} \propto D$; i.e., the resonance regions, and therefore the gain, are limited by the size of the focal spot (≈40 and 60 μm, respectively). By contrast, in the RPP2-S shots, where $D > L'_{res}$, SSRS growth is limited by the curvature of the plasma ($L'_{res} \approx 70$ μm).

This picture satisfactorily explains the relative values of SSRS intensities $I_{SSRS} \propto e^{\Gamma_{SSRS}}$ obtained in the different RPP configurations, where $I_{SSRS}^{RPP2P} \ll I_{SSRS}^{RPP1} \lesssim I_{SSRS}^{RPP2S}$. Approximating the laser intensity as constant across the spot (≈FWHM) and applying again the model of Mostrom and Kaufmann,[3] we obtain gains for λ_{SSRS} = 700 nm of $\Gamma_{SSRS} \approx 6$, 8.7, and 9.4 for RPP2-P, RPP1, and RPP2-S spots, respectively, resulting in I_{SSRS} enhancements of ≈15 and ≈2, going from the smaller to the larger FHWM spot. This is consistent with the experimental values.

A more detailed calculation of the gain could be obtained by modeling the ray-tracing of SSRS light in the time-varying 2D density maps. It is worth noting that the SSRS intensity observed for the RPP2-S shots cannot be explained without accounting for the plasma curvature, unless a mechanism of saturation is active. We also remark that the above interaction conditions imply that eigenmodes, i.e., absolute SSRS solutions, cannot grow in this experiment. According to Ref. 3, in fact, these modes prevail for times longer than t_s and require a laser beam larger than $2L_{res} \approx 240$ μm.

The limiting factors of SSRS growth discussed above suggest also a plausible explanation for the confinement of SSRS to densities higher than $0.13n_c$ in the RPP2-P case. Since the resonance L_{res} increases toward lower plasma densities, rising from ≈80 μm for $n_e = 0.16n_c$ to ≈190 μm for $n_e = 0.08n_c$, the size of the beam (D = 40 μm) will be a stronger limiting factor at lower densities, resulting in a negligible level of gain.

Unlike SSRS, the shape of the focal spot does not affect the growth of BSRS. FAB calorimetry for RPP2 shots on thick targets yielded a BSRS reflectivity of ~ (0.025 ± 0.005)%, which is comparable to the value obtained with RPP1. Consistently, similar BSRS intensities were measured by the FAB streak camera, with average values differing by 50% in the two irradiation conditions, which is less than the shot-to-shot reproducibility. This result is expected, since BSRS grows convectively in the backward direction, and the gain is therefore not affected by laser spot size. According to the Rosenbluth model,[26] the linear BSRS gain $\Gamma_{BSRS} \propto L_n I$. Small variations of total BSRS reflectivity in RPP1 and RPP2 irradiation can therefore be produced by the different intensity profiles of the laser beam in the two cases.

Confirmation of the different roles played by L_n in the growth of SSRS and BSRS was obtained from the shots on thin foil targets of different thickness. A typical angularly resolved spectrum from a 2 μm target irradiated using RPP1 is shown in Fig. 8, while the scattered energies at different angles are plotted in Fig. 4(d). It is interesting to note that the $\omega_0/2$ signal is still visible in the spectrum; this is confirmed by the FAB streak camera, revealing that TPD disappears at a time 100–150 ps after the laser peak, different from the profile reported in Fig. 5(b). Hydrodynamic simulations show in fact that the peak electron density falls below n_c before the laser peak, and below $n_c/4$ ~100 ps after the laser peak, as shown in Fig. 2(a). n-BSRS is again observed in Fig. 8 in both the P- and S-planes with comparable intensity; the signal, however, is much higher than that

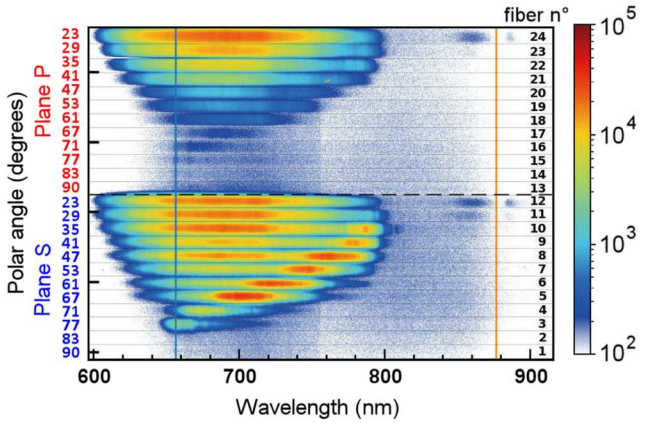

FIG. 8. Angularly resolved spectrum from a 2 μm Parylene-N target obtained using the circular focal spot (RPP1) with peak laser intensity $I = 0.9 \times 10^{16}$ W/cm^2. The vertical orange line indicates the $\omega_0/2$ wavelength.

obtained on thick targets (Fig. 3). By comparing the spectra obtained for different foil targets in RPP1 shots, we observe that the n-BSRS intensity falls with increasing target thickness, approaching that measured for thick targets [Fig. 7(b)]. Consistently, the pyroelectric detector in the FAB cone measured an average BSRS reflectivity with RPP1 of $(0.14 \pm 0.01)\%$, $(0.08 \pm 0.01)\%$, and $(0.015 \pm 0.010)\%$ for 2, 3, and 5 μm foils, respectively, compared with $(0.020 \pm 0.005)\%$ obtained for thick targets [green triangles in Fig. 7(b)]. A similar trend was obtained by using RPP2, where calorimetry of BSRS showed a fall by a factor ~60 on passing from 2 μm foils to thick targets. The enhancement of n-BSRS in foil targets can be also observed in Figs. 4(b) and 4(d), reporting the angularly resolved scattered energies measured in RPP2-P and RPP2-S shots on 2 μm targets. All the curves plotted from thin foils, in fact, exhibit a decreasing trend of scattered energy vs angle, implying that n-BSRS, stronger at low polar angles, dominates over SSRS; in the S-plane, however, the scattered energy remains higher at larger angles, owing to the contribution of SSRS. The trends described above confirm the strong dependence of BSRS and n-BSRS on L_n, as expected from the Rosenbluth theory.

The SSRS spectrum is also visible in Fig. 8 and clearly distinguishable in the S-plane, showing features similar to those in Fig. 3. The total intensity is shown in Fig. 7(b) for different targets. Despite the poor reproducibility, the statistical average of SSRS intensity is comparable for all the targets, confirming that its growth is not affected by the density scale length. As discussed above, this follows from the fact that the effective resonance length is dictated by the laser spot size or by the plasma curvature. Similar information on SSRS can be obtained by comparing the energy curves in the S-planes in Figs. 4(d) and 4(f) with those in Figs. 4(c) and 4(e), corresponding to thick targets. It is evident that the maximum value of the scattered energy is similar in the two cases; however, for thick targets, the curve decreases at smaller angles, owing to the lower contribution of n-BSRS.

In conclusion, angularly and spectrally resolved measurements of scattered light have allowed us to obtain a detailed characterization of BSRS, n-BSRS, SSRS, and TPD at laser intensities relevant to the shock ignition scheme for ICF. Variation of focal spot geometry and target thickness have allowed investigation of the dependence of BSRS and SSRS on the spot features and on the electron density scale length of the plasma. While BSRS (and n-BSRS) scales with L_n, as expected from linear theory, SSRS has been shown to be insensitive to L_n and to increase with the extent of the focal spot in the S-direction, which is the most favorable direction of growth. Consistently, the measured SSRS signal is much stronger in the S-plane than in the P-plane. This implies that the resonance length of convective SSRS is limited by the size of the laser spot or by the plasma curvature, and is therefore smaller than the value calculated for a planar infinite plasma, which scales with L_n.

It is worth remarking that both the density scale length and the focal spot size are here much smaller than the values envisaged in realistic ICF conditions. As BSRS reflectivity is expected to boost to tens of percent in plasma coronas of hundreds of micrometers length at intensities ~ 10^{16} W/cm^2, SSRS can also become much stronger for larger laser spots, which are needed to obtain homogeneous laser irradiation of the fuel capsule. The results presented above suggest that estimation of SSRS reflectivity must account for realistic irradiation conditions and 2D plasma profiles; this holds in particular at lower plasma densities, where the size of the beam and the radius of curvature of the plasma, both of the order of a millimeter, become comparable to the resonance length, thus strongly limiting SSRS growth.

We would like to thank J. Myatt, P. Michel, and D. Carleton for useful discussions and valuable suggestions. We would like to acknowledge financial support from the LASERLAB-EUROPE Access to Research Infrastructure Activity (Application No. 23068). This work has also been carried out within the framework of EUROfusion Enabling Research Projects AWP21-ENR-01-CEA-02 and AWP24-ENR-IFE-02-CEA-02, and has received funding from Euratom Research and Training Programme 2021–2025 under Grant No. 633053. The views and opinions expressed herein do not necessarily reflect those of the European Commission. We also acknowledge the NextGeneration EU Integrated Infrastructure I-PHOQS—Initiative in Photonic and Quantum Sciences (CUP B53C22001750006, ID D2B8D520, and IR0000016). This work is also supported by the Ministry of Youth and Sports of the Czech Republic [Project No. LM2023068 (PALS RI)] and by the Strategic Priority Research Program of the Chinese Academy of Sciences (Grant Nos. XDA25030200 and XDA25010100). This work has been supported by COST (European Cooperation in Science and Technology) through Action CA21128 PROBONO (PROton BOron Nuclear Fusion: from energy production to medical applicatiOns).

AUTHOR DECLARATIONS

Conflict of Interest

The authors have no conflicts to disclose.

Author Contributions

G. Cristoforetti: Conceptualization (lead); Data curation (equal); Formal analysis (equal); Funding acquisition (lead); Investigation (equal); Project administration (lead); Resources (equal); Supervision (equal); Visualization (equal); Writing – original draft (equal); Writing – review & editing (equal). **E. Hume**: Data curation (equal); Formal analysis (equal); Investigation (equal); Visualization (equal); Writing – review & editing (equal). **S. Agarwal**: Data curation (equal); Formal analysis (equal); Investigation (equal); Resources (equal). **D. Batani**: Funding acquisition (equal); Supervision (equal); Visualization (equal); Writing – review & editing (equal). **M. Cervenak**: Data curation (equal); Investigation (equal); Resources (equal). **P. Devi**: Data curation (equal); Investigation (equal). **R. Dudzak**: Resources (equal). **D. Ettel**: Investigation (equal); Resources (equal). **P. Gajdos**: Investigation (equal); Resources (equal). **K. Glize**: Conceptualization (equal); Data curation (equal); Formal analysis (equal); Investigation (equal); Resources (equal); Writing – review & editing (equal). **S. Jelinek**: Data curation (equal); Formal analysis (equal); Investigation (equal). **L. Juha**: Funding acquisition (equal); Project administration (equal); Resources (equal); Supervision (equal). **P. Koester**: Conceptualization (equal); Data curation (equal); Investigation (equal); Supervision (equal); Writing – review & editing (equal). **M. Krupka**: Data curation (equal); Formal analysis (equal); Investigation (equal); Resources (equal). **M. Krus**: Funding acquisition (equal); Project administration (equal);

Resources (equal); Supervision (equal). **H. Larreur**: Data curation (equal); Investigation (equal). **G. Malka**: Data curation (equal); Formal analysis (equal); Investigation (equal); Writing – review & editing (equal). **D. Mancelli**: Data curation (equal); Investigation (equal). **P. E. Masson-Laborde**: Formal analysis (equal); Software (equal). **A. Morace**: Resources (equal); Supervision (equal). **Ph. Nicolai**: Formal analysis (equal); Software (equal); Writing – review & editing (equal). **O. Renner**: Data curation (equal); Formal analysis (equal); Investigation (equal); Writing – review & editing (equal). **D. Singappuli**: Data curation (equal); Investigation (equal). **S. Singh**: Data curation (equal); Formal analysis (equal); Investigation (equal); Writing – review & editing (equal). **M. Tatarakis**: Formal analysis (equal); Supervision (equal). **X. Yuan**: Funding acquisition (equal); Supervision (equal). **Y. Wang**: Data curation (equal); Formal analysis (equal); Investigation (equal); Resources (equal). **N. Woolsey**: Formal analysis (equal); Resources (equal); Supervision (equal); Writing – review & editing (equal). **J. Zhang**: Funding acquisition (equal); Supervision (equal). **X. Zhao**: Data curation (equal); Formal analysis (equal); Investigation (equal); Resources (equal). **L. A. Gizzi**: Conceptualization (equal); Funding acquisition (equal); Project administration (equal); Resources (equal); Supervision (equal); Writing – review & editing (equal).

DATA AVAILABILITY

The data that support the findings of this study are available from the corresponding author upon reasonable request.

REFERENCES

[1] C. S. Liu, M. N. Rosenbluth, and R. B. White, "Parametric scattering instabilities in inhomogeneous plasmas," Phys. Rev. Lett. **31**, 697 (1973).

[2] B. B. Afeyan and E. A. Williams, "Stimulated Raman sidescattering with the effects of oblique incidence," Phys. Fluids **28**, 3397 (1985).

[3] M. Mostrom and A. Kaufmann, "Trapped modes in acoustic waveguides," Phys. Rev. Lett. **42**, 644 (1979).

[4] P. Michel, *Introduction to Laser Plasma Interactions* (Springer, 2013).

[5] R. P. Drake, R. E. Turner, B. F. Lasinski, K. G. Estabrook, E. M. Campbell *et al.*, "Efficient Raman sidescatter and hot-electron production in laser–plasma interaction experiments," Phys. Rev. Lett. **53**, 1739 (1984).

[6] R. P. Drake, R. E. Turner, B. F. Lasinski, E. A. Williams, D. W. Phillion *et al.*, "Studies of Raman scattering from overdense targets irradiated by several kilojoules of 0.53 μm laser light," Phys. Fluids **31**, 3130–3142 (1988).

[7] R. P. Drake, "The scaling of absolutely unstable, stimulated Raman scattering from planar, laser-produced plasmas," Phys. Fluids B **1**, 1082–1088 (1989).

[8] M. J. Rosenberg, A. A. Solodov, J. F. Myatt, W. Seka, P. Michel *et al.*, "Origins and scaling of hot-electron preheat in ignition-scale direct-drive inertial confinement fusion experiments," Phys. Rev. Lett. **120**, 055001 (2018).

[9] M. J. Rosenberg, A. A. Solodov, W. Seka, R. K. Follett, J. F. Myatt *et al.*, "Stimulated Raman scattering mechanisms and scaling behavior in planar direct-drive experiments at the National Ignition Facility," Phys. Plasmas **27**, 042705 (2020).

[10] P. Michel, M. J. Rosenberg, W. Seka, A. A. Solodov, R. W. Short *et al.*, "Theory and measurements of convective Raman side scatter in inertial confinement fusion experiments," Phys. Rev. E **99**, 033203 (2019).

[11] S. Hironaka, J. Sivajeyan, J. Wang, M. J. Rosenberg, A. Solodov *et al.*, "Identification of stimulated Raman side scattering in near-spherical coronal plasmas on OMEGA EP," Phys. Plasmas **30**, 022708 (2023).

[12] K. Glize, X. Zhao, Y. H. Zhang, C. W. Lian, S. Tan *et al.*, "Measurement of stimulated Raman side-scattering predominance in directly driven experiment," Phys. Plasmas **30**, 122706 (2023).

[13] X. Zhao, X. H. Yuan, J. Zheng, Y. F. Dong, K. Glize *et al.*, "An angular-resolved scattered-light diagnostic for laser-plasma instability studies," Rev. Sci. Instrum. **93**, 053505 (2022).

[14] Y. Zhang, Z. Zhang, X. Yuan, K. Glize, X. Zhao *et al.*, "Efficient energy transport throughout conical implosions," Phys. Rev. E **109**, 035205 (2024).

[15] X. Zhao, X. H. Yuan, Y. F. Dong, K. Glize, Y. H. Zhang *et al.*, "Measurements of laser-plasma instabilities in double-cone ignition experiments relevant to the direct-drive conditions at Shenguang-II Upgrade laser facility," Nucl. Fusion **64**, 086069 (2024).

[16] C. Z. Xiao, H. B. Zhuo, Y. Yin, Z. J. Liu, C. Y. Zheng *et al.*, "On the stimulated Raman sidescattering in inhomogeneous plasmas: Revisit of linear theory and three-dimensional particle-in-cell simulations," Plasma Phys. Controlled Fusion **60**, 025020 (2018).

[17] C. Z. Xiao, Q. Wang, and J. F. Myatt, "*k*-space theory and convective gains of stimulated Raman side scattering," Phys. Rev. E **107**, 025203 (2023).

[18] C. Z. Xiao, Q. Wang, and J. F. Myatt, "Evaluating the importance of Raman and Brillouin side scattering at ignition conditions," Phys. Plasmas **30**, 072702 (2023).

[19] G. Cristoforetti, L. Antonelli, D. Mancelli, S. Atzeni, F. Baffigi *et al.*, "Time evolution of stimulated Raman scattering and two-plasmon decay at laser intensities relevant for shock ignition in a hot plasma," High Power Laser Sci. Eng. **7**, e51 (2019).

[20] L. A. Gizzi, D. Giulietti, A. Giulietti, T. Afshar-Rad, V. Biancalana *et al.*, "Characterization of laser plasmas for interaction studies," Phys. Rev. E **49**, 5628–5643 (1994).

[21] J. Breil, S. Galera, and P. H. Maire, Comput. Fluids **46**, 161 (2011).

[22] E. Lefebvre, S. Bernard, C. Esnault, P. Gauthier, A. Grisollet *et al.*, "Development and validation of the TROLL radiation-hydrodynamics code for 3D hohlraum calculations," Nucl. Fusion **59**, 032010 (2018).

[23] G. Cristoforetti, A. Colaïtis, L. Antonelli, S. Atzeni, F. Baffigi *et al.*, Europhys. Lett. **117**, 35001 (2017).

[24] G. Cristoforetti, L. Antonelli, S. Atzeni, F. Baffigi, F. Barbato *et al.*, "Measurements of parametric instabilities at laser intensities relevant to strong shock generation," Phys. Plasmas **25**, 012702 (2018).

[25] Q. Wang, C. Z. Xiao, Y. Xie, H. B. Cai, J. Chen *et al.*, "PIC simulations of the competition between backward and forward stimulated Raman side scatter in ignition-scale direct-drive coronal conditions," Phys. Plasmas **31**, 042710 (2024).

[26] M. N. Rosenbluth, "Parametric instabilities in inhomogeneous media," Phys. Rev. Lett. **29**, 565–567 (1972).